

Terahertz-frequency carrier dynamics and spectral weight redistribution in the nearly magnetic metal CaRuO_3

Saeid Kamal,¹ D. M. Kim,² C. B. Eom,² and J. S. Dodge¹¹*Department of Physics, Simon Fraser University, Burnaby, BC V5A 1S6, Canada*²*Department of Material Science and Engineering, University of Wisconsin-Madison, Madison, Wisconsin 53706, USA*

(Received 27 June 2006; published 25 October 2006)

We present measurements of the low-frequency optical conductivity of epitaxial thin films of CaRuO_3 , obtained with time-domain terahertz spectroscopy. We resolve a narrow conductivity peak near $\omega=0$ that deviates from Drude dynamics down to very low frequencies. By determining the spectral weight of this feature we estimate that the carrier kinetic energy changes by 0.2 eV per site upon cooling from room temperature and, where measurements are available, the strength of this change correlates well with magnetism in three-dimensional ruthenium oxides. We show that the time-domain terahertz technique provides a precise measure of the optical mass renormalization in extended Drude analysis and we show that this turns up sharply as the temperature is reduced below 50 K. We express our results in terms of a distribution of scattering rates and show how this description relates to other approaches in the literature. Our measurements are consistent with an anomalous power law description over a narrow range of frequencies and temperatures but significant deviations are observed and discussed. We show that our results are not described by a ω/T scaling form.

DOI: [10.1103/PhysRevB.74.165115](https://doi.org/10.1103/PhysRevB.74.165115)

PACS number(s): 78.20.-e, 71.27.+a, 71.38.Cn, 78.30.-j

I. INTRODUCTION

The paramagnetic metal CaRuO_3 exhibits neither magnetic order nor superconductivity, but it is one of the most intriguing members of the ruthenium oxide family.¹ Its resistivity behaves as $\rho \propto \sqrt{T}$ at high temperatures, in contrast with the linear temperature dependence that normally results from electron-phonon scattering.² At low temperatures the resistivity crosses over to $\rho \propto T^{3/2}$, with no evidence of the T^2 dependence expected of a Fermi liquid, even at the lowest temperatures.^{2,3} Infrared spectroscopy has revealed that at high temperatures, the metallic conductivity has a local minimum at $\omega=0$, suggestive of incomplete gap formation in the electronic density of states near the Fermi level.⁴ As temperature decreases, the conductivity at low frequencies grows in strength, eventually developing a peak at $\omega=0$ that appears to decay as $\sigma_1 \propto 1/\sqrt{\omega}$ at high frequencies,⁴ in contrast with the conventional Drude law $\sigma_1 \propto 1/\omega^2$. The defining characteristic of a metal is its ability to transport charge from one place to another, and the optical conductivity measures how easily this occurs,⁵ so these anomalies represent fundamental challenges to our understanding of metals.

Equally anomalous phenomenology has been observed in other materials, including the itinerant ferromagnets SrRuO_3 (Ref. 6) and MnSi ,⁷ as well as optimally doped cuprate superconductors.⁸ All of these materials exhibit dynamics on multiple time scales, in contrast with the single time scale reflected in Drude dynamics, and this presents significant methodological challenges for interpreting the results of conductivity measurements.⁹ Fundamentally different physical models can often yield remarkably similar predictions for the temperature and frequency dependence of the conductivity, making careful quantitative analysis essential for discriminating among competing theoretical proposals. Fermi liquid theory predicts that the free carriers should ultimately exhibit Drude dynamics at low energy scales, so experimental results at low frequencies and temperatures are significant.

In this work we present terahertz time-domain spectroscopy (THz-TDS) measurements of the conductivity in CaRuO_3 at millivolt energy scales. We find that the free-carrier conductivity of CaRuO_3 deviates from Drude response throughout our low-frequency bandwidth, and possesses a spectral weight that is both strongly temperature dependent and renormalized from band theory. As the temperature is increased, this spectral weight is reduced by selectively depleting a narrow conductivity peak that sits on top of a broad, relatively temperature-independent background, and we associate the strength of this change with the tendency toward ferromagnetism. Below $T \sim 50$ K we find that the conductivity peak narrows significantly, indicating the appearance of a new low-temperature time scale $\tau \sim 300$ fs, much longer than band theory would predict for this metal. We describe a multicomponent approach to conductivity analysis that focuses attention on experimentally measured time scales and complements existing methods. We assess theoretical models based on anomalous power-law dynamics^{6,7,10,11} and quantum critical scaling^{4,8} in light of insights obtained with this approach.

In Sec. II we describe the experimental technique and present the raw conductivity data that forms the basis for our discussion. In Sec. III we summarize relevant features of the electronic structure of CaRuO_3 . Section IV discusses our measurements from a variety of phenomenological viewpoints. Section IV A shows that our results are incompatible with a simple Drude law at low frequencies. Section IV B provides an overview of methods used in the literature to characterize metals that are not simply described by a Drude model. Section IV C describes how spectral weight is redistributed as temperature is varied and presents some of the unique features that THz-TDS provides for determining this. In this section we also connect the temperature dependence of the spectral weight to the tendency toward magnetism in ruthenium oxides. Section IV D presents our multicomponent analysis and compares it with common alternatives. In

Sec. IV E we present a scaling analysis of our results. We find that the scaling hypothesis is not satisfied by our data, but that this is not evident from a conventional scaling plot; we discuss the significance of this observation for the ongoing effort to apply quantum critical scaling analysis to other materials. We conclude in Sec. V.

II. EXPERIMENT

With THz-TDS we measure $\tilde{\tau}_r(\omega)$, the complex transmission amplitude of epitaxial CaRuO₃ films, relative to a matched substrate reference.¹² Film thicknesses ranged between 40–50 nm, and were deposited by 90° off-axis sputtering techniques on 4° miscut (110) NdGaO₃ substrates that had dimensions $15 \times 15 \times 1$ mm³.^{13–15} The substrate miscut is toward the $\langle \bar{1}10 \rangle$ in-plane direction of the substrates and promotes single domain formation in CaRuO₃.^{16,17} Furthermore, high miscut angle substrates stabilize volatile Ru and maintain stoichiometry on the short terrace lengths of the surfaces. The $\langle \bar{1}10 \rangle$ in-plane direction of the CaRuO₃ lies parallel with $\langle \bar{1}10 \rangle$ and miscut direction of the (110) NdGaO₃ substrates. The large sample area is used to avoid spurious signals that can result from radiation scattered from sample edges, and is not indicative of the probe area; the actual $1/e$ field diameter at the focus is only a few millimeters at 0.2 THz, and smaller for higher frequencies.

Although we have studied several samples, their features are broadly consistent; so we limit our discussion to THz-TDS measurements of a single sample that we have studied in great detail. The inset to Fig. 1 shows its resistivity, determined with the van der Pauw method. The residual resistivity of $42 \mu\Omega$ cm at $T=5$ K is ten times larger than that of the best available single crystals,³ and about 30% higher than the films studied with infrared reflectance by Lee *et al.*,⁴ fabricated using the same deposition technique but on different substrates. Experimental evidence on other oxides indicates that this level of disorder primarily affects states at very low energies, well below the 0.5 meV lower bound of our frequency and temperature range. In earlier work on SrRuO₃, for example, THz-TDS measurements on samples with residual resistivity $\rho_0 \sim 50 \mu\Omega$ cm agreed well with the infrared conductivity at $\nu=100$ cm⁻¹ of samples with more than an order of magnitude lower residual resistivity. Similarly, the normal state properties of copper oxide materials are relatively insensitive to the moderate levels of disorder associated with thin films, despite the strong disorder dependence of the superconducting properties.^{18,19} As shown by Capogna *et al.*,³ however, disorder does become relevant to the metallic properties of ruthenium oxides if one tries to rely on terahertz measurements to extrapolate $\tilde{\sigma}(\omega)$ to low temperatures and frequencies.

Recent work indicates that the electrical properties of CaRuO₃ exhibit measurable anisotropy,^{20,21} whereas the infrared measurements were performed with unpolarized light.²² In a preliminary study, we have found no evidence for anisotropic THz conductivity at room temperature within about 3% rms uncertainty, contrary to the prediction of density functional theory (DFT) calculations.²¹ However, trans-

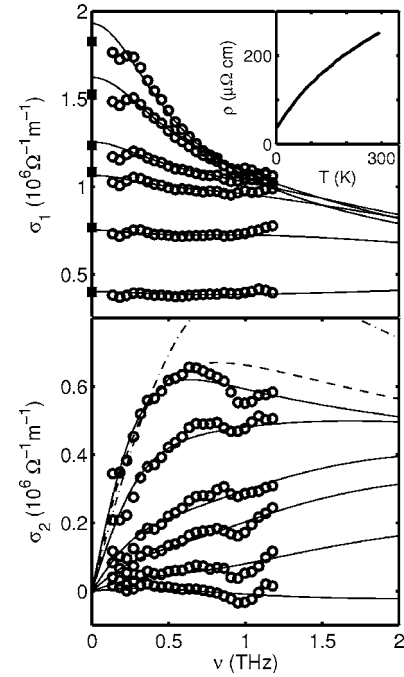


FIG. 1. Real and imaginary part of the *ab*-plane conductivity of CaRuO₃ for $T=16, 25, 40, 50, 90,$ and 290 K, from top to bottom, respectively. Square markers on the abscissa indicate dc measurements on the same sample, shown in more detail in the inset. The combined statistical and systematic uncertainty over 0.25 – 0.8 THz is approximately the marker size. Outside this range, systematic uncertainty associated with the discrete Fourier transform becomes noticeable as small oscillations in the data; the amplitude indicates the size of the uncertainty. Solid lines are best fits to the data of Eq. (11) plus a Lorentzian. Dashed lines shown in the lower panel are fits to the $T=16$ K data using two alternative forms: a single Drude peak, Eq. (1), fit to the restricted range $\nu < 0.5$ THz (short dashes), and the anomalous power law form given by Eq. (3) (long dashes).

port measurements show that the residual resistivity ratio is anisotropic, so apparently the anisotropy grows with temperature.²⁰ We will discuss this anisotropy and its temperature dependence in subsequent work, but it does not appear to be enough to undermine a useful comparison between our polarized measurements and the unpolarized infrared work, as long as we recognize that the *c*-axis contribution to the infrared measurements may produce as much as 50% more conductivity at low temperatures than the THz measurements described here;²¹ in which the electric field vector was along the $\langle 1\bar{1}0 \rangle$ direction of the orthorhombic CaRuO₃ unit cell.

From $\tilde{\tau}_r(\omega)$, we determine both the real and imaginary parts of the complex conductivity, $\tilde{\sigma}(\omega) = \sigma_1(\omega) + i\sigma_2(\omega)$, by inverting the Tinkham formula for thin-film transmission.¹² No Kramers-Kronig transformation is required, and the measurement technique is both reproducible and precise, at frequencies $\nu=0.1$ – 1.2 THz that are difficult to access with conventional methods. Prior to film deposition, we measured $\tilde{\tau}_r(\omega)$ of sample substrates relative to the same reference, to reduce systematic uncertainty associated with substrate mismatch. This allows us to determine the relative phase delay between the sample and reference to an accuracy of a few

femtoseconds. The relative phase delay $\arg[\tilde{\epsilon}_r]$ is approximately related to the conductivity phase angle $\arg[\tilde{\sigma}(\omega)]$, while the amplitude $|\tilde{\epsilon}_r|$ is approximately related to $|\tilde{\sigma}(\omega)|$. Hence, the accuracy of our delay implies that $\arg[\tilde{\sigma}(\omega)]$ is determined to better than ± 0.01 rad over the range 0.3–1.0 THz, three times better than the systematic uncertainty achieved in earlier work on SrRuO₃.⁶ Moreover, the variation of $d\sigma_2/d\omega$ with temperature in CaRuO₃ is about a factor of 2 greater than it is in SrRuO₃, so our relative uncertainty for this important quantity is six times better than previous measurements.

THz-TDS measurements at representative temperatures are shown in Fig. 1. The measurements extrapolate well to the dc values, although this may be fortuitous given the expected anisotropy and variation in quality over the 15×15 mm² sample area probed in the resistivity measurement. The real part of the conductivity is relatively flat with frequency above $T \approx 100$ K, with a weak but measurable positive curvature that is most evident for the $T = 90$ K data. Below this temperature scale, σ_1 develops a strong frequency dependence; at $T = 16$ K, the variation between dc and 1 THz nearly reaches a factor of 2. For a metal with $\rho_0 \sim 40 \mu\Omega$ cm, this indicates a remarkably low scattering rate, much lower than that observed in SrRuO₃ samples with comparable residual resistivities, and among the strongest observed in oxide metals.^{6,23} The variation of $\sigma_2(\omega)$ is even stronger, exhibiting a maximum near 0.6 THz at low temperatures. Even at temperatures, for which $\sigma_1(\omega)$ is essentially constant, $\sigma_2(\omega)$ still exhibits measurable variation; and this will play an important role in our subsequent analysis.

At the high-frequency end of the THz-TDS spectrum, the signal strength decays exponentially with frequency, and spectral leakage in the discrete Fourier transform begins to become a significant source of systematic uncertainty in determining the conductivity. Conversely, at the low-frequency end of the infrared reflectance spectra, the Kramers-Kronig analysis becomes sensitive to the choice of low-frequency extrapolation. Also, as temperature is reduced and the low-frequency reflectance approaches unity, the effect of measurement inaccuracy is amplified. We characterize these uncertainties by comparing THz-TDS measurements to the infrared reflectance results of Lee *et al.*,⁴ as shown in Fig. 2 with both linear and logarithmic frequency scales.

The quality of the agreement strengthens confidence in both sets of measurements: both methods indicate that the conductivity possesses a weak minimum at zero frequency for temperatures above 100 K, with spectral weight building up at low frequencies as the temperature is reduced. Below $T \sim 100$ K, the local minimum at $\sigma_1(\omega=0)$ becomes a local maximum, and the temperature-dependent peak observed in infrared reflectance becomes a shoulder. The two data sets exhibit small mismatches at the two lowest temperatures, and while it is likely that some of this is due to a combination of sample variation, measurement uncertainty, and differences between unpolarized IR measurements and polarized THz measurements, the basic phenomenology that we have described is well within these systematic uncertainties.

The logarithmic frequency scale in the inset of Fig. 2 draws attention to details of $\tilde{\sigma}(\omega)$ that were not addressed in

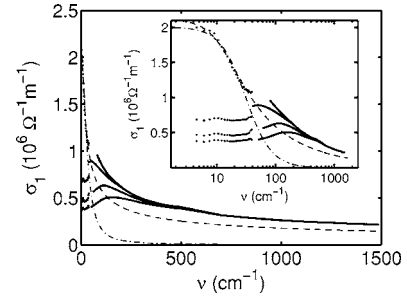


FIG. 2. Real part of conductivity for $T = 10, 100, 200,$ and 300 K. Discrete points are from THz-TDS measurements described here, and lines are from infrared reflectance measurements of Lee *et al.* (Ref. 4). The same data is reproduced in the inset with a logarithmic frequency scale for easier comparison at low frequencies.

earlier work. At low temperatures the conductivity develops considerable structure that is inaccessible to IR reflectance spectroscopy, for reasons that we discuss in Sec. IV C. This peak is not described at all by a simple Drude response, and one of the important contributions of this work is a detailed experimental characterization of the multiple time scales that it reflects. This is related to the problem of characterizing multiple exponential decays in the time domain; indeed, a Drude peak in the frequency domain reflects nothing more than an impulse response with single-sided exponential decay in the time domain, and in both domains a logarithmic scale ensures that the experimental measurements are given appropriate weight. As the inset to Fig. 2 emphasizes, our measurements provide detail over an entire decade of frequency that was unavailable previously.

III. ELECTRONIC STRUCTURE

Here we give a brief review of the electronic properties of CaRuO₃,^{21,24} to provide context for the discussion to follow. Figure 3 shows the orbitals responsible for metallic conduction in the ruthenium oxide plane. In an ionic picture, the oxygen orbitals are filled, and ligand-field interactions split the orbital manifolds with t_{2g} and e_g symmetry by 2 eV, so the four electrons in the Ru(4d) orbital are in a low-spin state. Hybridization promotes charge transfer between the

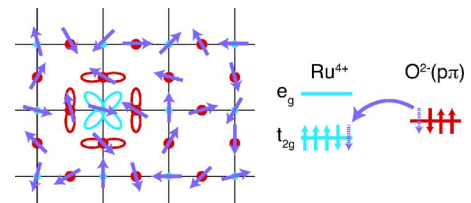


FIG. 3. (Color online) Schematic of the relevant orbitals in a ruthenium oxide plane. Ruthenium atoms at the corners of the pseudocubic lattice are π -bonded with oxygen atoms on the cubic cell edges. Hybridization induces electron transfer from O(2p) to Ru(4d) orbitals with t_{2g} symmetry, so that on average there are five electrons (one t_{2g} hole) in Ru(4d) states and 1/3 of a hole in each O(2p) orbital.

O($2p$) to Ru($4d$) orbitals, and the resulting charge distribution balances the onsite Coulomb repulsion energy of each atom. An average of five electrons occupy the Ru($4d$) atoms in local spin density calculations, leaving a single hole to be distributed among the three oxygen atoms in the formula unit.²¹

Each ruthenium atom sits on three mutually orthogonal planes, one for each t_{2g} orbital. The bonding arrangement in each of these planes would be identical if it were not for the perovskite distortion. This imposes a strong two-dimensional character on the electronic states of CaRuO₃ and SrRuO₃, despite their three-dimensional crystal structures. The lower dimensionality is reflected in the band structure of the ideal cubic structure by flat bands along certain directions and by a nested Fermi surface that resembles three intersecting cylinders.²⁴ In CaRuO₃ this nesting presumably produces magnetic fluctuations at finite \mathbf{q} that are at least partially responsible for its antiferromagnetic Weiss temperature, obtained from high-temperature extrapolation of the magnetic susceptibility.²⁵ For many years this negative Weiss temperature was understood as evidence for the dominance of antiferromagnetic interactions in CaRuO₃, but recent work has shown that this compound is nearly *ferromagnetic*, very similar to palladium.^{21,26–28} This is consistent with the enhanced effective mass observed in specific heat $m^*/m_b \cong 10$ and with the unusually large value of the Wilson ratio $R \cong 10$.^{21,26,29}

Band structure calculations associate this tendency to ferromagnetism with a Stoner mechanism, resulting from a large density of states at the Fermi level.²¹ That these states have about 1/3 oxygen character plays an important role because the Stoner parameter of oxygen is large, and because the bonding arrangement favors ferromagnetism over an instability at finite \mathbf{q} : with commensurate antiferromagnetic order in the ruthenium sublattice, the oxygen orbitals must have zero spin polarization by symmetry, preventing them from contributing magnetic energy.

IV. DISCUSSION

In a hypothetical metal with no disorder, $\sigma_1(\omega)$ has a delta function centered at zero frequency, and analysis is straightforward: the amplitude of the delta function relates directly to the charge stiffness of the metal, and all other features of the conductivity are related to interband transitions that do not transport charge over macroscopic distances.⁵ But real materials are not so simple. Disorder inevitably broadens the delta function response, and to make progress, further phenomenological analysis is required to connect physical processes to the raw conductivity data. In this section we critically examine the application of several analytical frameworks to our measurements of $\bar{\sigma}(\omega)$ in CaRuO₃, and discuss the physical inferences that result.

A. Inadequacy of the Drude model

In many metals, including even quite complex heavy fermion compounds,³⁰ the effect of static and thermally-induced

disorder can be remedied by replacing the delta function response with a narrow Drude peak

$$\bar{\sigma}(\omega) = \frac{\epsilon_0 \omega_p^2}{\gamma - i\omega}. \quad (1)$$

A complex least-squares fit of a Drude form to the 16 K data over the restricted range $\nu < 0.5$ THz is shown with short dashed lines in Fig. 1. In this and all other complex fits to THz-TDS data, we vary the parameters to minimize the sum of the squared error $|\sigma_{1,\text{model}} - \sigma_{1,\text{data}}|^2 + |\sigma_{2,\text{model}} - \sigma_{2,\text{data}}|^2$ over the frequency range shown. The THz-TDS data clearly deviate from the fits at high frequencies, with the most pronounced discrepancy appearing in $\sigma_2(\omega)$. Discrepancies with Drude conductivity are also evident at high temperatures. At room temperature, for example, σ_1 increases weakly with frequency; at the same temperatures, σ_2 increases weakly with frequency below 0.4 THz, but then drops below zero above 0.5 THz.

Neither of these features can be obtained with simple Drude conductivity, for which $\sigma_1(\omega)$ decreases monotonically with frequency and $\sigma_2(\omega)$ is nonnegative. All of these features indicate excess spectral weight in $\sigma_1(\omega)$ in the mid-infrared (mid-IR), identified by Lee *et al.*⁴ and clearly observable in Fig. 2. Although this excess weight lies primarily outside of the THz-TDS bandwidth, it influences $\sigma_2(\omega)$ within the THz-TDS bandwidth by virtue of the Kramers-Kronig relations, as we discuss in Sec. IV C. We emphasize that the energy scale of these deviations is 5 meV (1.25 THz) and below.

B. Overview of optical conductivity models

Excess mid-IR conductivity is exhibited by many oxide metals, including cuprates,⁹ manganites,³¹ and other ruthenates.^{6,4,32,33} It is not obvious *a priori* that the mid-IR spectral weight of these materials has a common physical origin, but the technical problem that it is not easily distinguishable from a simple Drude response is common to all. Phenomenological approaches to this difficulty fall into roughly two categories: single-component models that treat all of the low-frequency conductivity as resulting from itinerant carriers, and multicomponent models that do not.⁹

Probably the most widely used single-component approach is the extended Drude model, obtained by simply allowing the relaxation rate γ in Eq. (1) to be complex and frequency dependent:^{9,34}

$$\bar{\sigma}(\omega) = \frac{\epsilon_0 \omega_p^2}{\gamma(\omega) - i\omega[1 + \lambda(\omega)]}. \quad (2)$$

The functions $\gamma(\omega)$ and $\lambda(\omega)$ can be obtained directly from the measured conductivity by inverting Eq. (2), within a scale factor set by uncertainty in ω_p^2 . This formulation has the virtue that under a few well-defined assumptions, these functions have immediate theoretical interest as the frequency-dependent momentum relaxation rate and mass renormalization, respectively.^{34–37} As discussed in Sec. IV C, THz-TDS can provide tight constraints on the low-frequency values of these quantities, and track their temperature dependence.³⁸

It is important to be aware of the assumptions associated with this interpretation, however.⁹ First, interband transitions should not contribute to the conductivity in Eq. (2). One may argue that this is well justified in some copper oxides that have a single band crossing the Fermi level, but as discussed in Sec. III ruthenium perovskites have three bands that cross the Fermi level; interband transitions between these bands are expected at low frequencies, and the strong spin-orbit coupling of the 4*d* ruthenium atoms will provide additional matrix elements to enhance their spectral weight. Elemental nickel, for example, exhibits mid-IR conductivity with a magnitude comparable to ruthenium oxides, in qualitative agreement with band structure calculations that include spin-orbit coupling.^{39,40} Furthermore, correlation effects can generate transitions even in a nominally single band material between extended states at the Fermi level and states in the upper Hubbard band.^{41,42} A more quantitative theoretical understanding of these issues for the ruthenium oxides is desirable, but does not yet exist.

A second assumption employed in the conventional interpretation of Eq. (2) is that the variation of the scattering rate over the Fermi surface is relatively small. If it is not, then the result of averaging over the distribution of scattering rates can modify the frequency dependence of the functions $\gamma(\omega)$ and $\lambda(\omega)$. In a notable example, Ioffe and Millis¹⁰ showed that if the scattering rate exhibits strong momentum dependence but no frequency dependence over a two-dimensional Fermi surface, the resulting low-frequency conductivity is given approximately by

$$\bar{\sigma}(\omega, T) = \frac{A}{[1/\tau(T) - i\omega]^\beta}, \quad (3)$$

where $\beta=1/2$ and A is temperature independent; all of the temperature dependence in $\bar{\sigma}(\omega, T)$ is given by $\tau(T)$, the maximum scattering lifetime over the Fermi surface. The power-law frequency dependence of Eq. (3) resembles the conductivity of layered copper oxides, and when it is expressed in terms of Eq. (2) it yields $\gamma(\omega)$ and $\lambda(\omega)$ with strong frequency dependence, despite the complete absence of frequency-dependent scattering and mass renormalization in the model.

Equation (3) was derived by assuming a two-dimensional Fermi surface and a specific functional form for the scattering rate anisotropy, so it is important to understand its generic features. To extend the analysis we express the conductivity as a weighted integral of Drude peaks with different scattering rates $\gamma=1/\tau$:

$$\bar{\sigma}(\omega) = \int_0^\infty d\gamma' \frac{\alpha(\gamma')}{\gamma' - i\omega}. \quad (4)$$

The basic physical content of Eq. (4) is that the carrier dynamics is described by a distribution of scattering rates $\alpha(\gamma)$, and is therefore not restricted to models that involve anisotropic scattering. However, in such a picture the amplitudes $\alpha(\gamma)$ are proportional to the amount of Fermi surface area that exhibits a scattering rate γ .

For the specific model proposed by Ioffe Millis,¹⁰ with a simple change of variable we obtain $\alpha(\gamma)$

$= 1/\sqrt{(\gamma - \gamma_{\min})(\gamma_{\max} - \gamma)}$, where γ_{\min} , γ_{\max} are the minimum and maximum scattering rates in the distribution, respectively. This distribution has square-root singularities at these extremal values because of the quadratic minima in the one-dimensional parametrization of the two-dimensional Fermi surface;⁴³ the $1/\sqrt{\omega}$ dependence of Eq. (3) is in turn a consequence of the singularity near γ_{\min} . Similar logic shows that to produce Eq. (3) with $\beta=1/2$ from anisotropic scattering in a three-dimensional system, the scattering rate should have lines of minima traversing the Fermi surface. We apply these ideas more fully to CaRuO₃ in Sec. IV D.

Sum rule analysis is a commonly used alternative to Eq. (2). It relies on the partial spectral weight of the optical conductivity, defined as

$$S(\Omega) = \frac{2}{\pi} \int_0^\Omega \sigma_1(\omega) d\omega. \quad (5)$$

If it is possible to choose the bandwidth Ω to include all intraband transitions and exclude all interband transitions, then in a tight-binding model the partial spectral weight provides a measure of the carrier kinetic energy

$$K(\Omega) = \frac{4\pi\epsilon_0 d}{e^2} S(\Omega), \quad (6)$$

where $d=V_{\text{cell}}^{1/3}$. This interpretation relies on the assumption that it is possible to find such a value of Ω , so despite the common characterization of Eq. (5) as model independent, in the presence of low-energy interband transitions its interpretation has methodological difficulties that are similar to those encountered with Eq. (2). A common choice is $\Omega \sim W$, where W is the electronic bandwidth taken from a band structure calculation.

Model calculations indicate that strong correlations can shift spectral weight over an unusually wide range of energies, greater than the electronic bandwidth.⁴¹ This is supported by experiments on oxide metals that observe temperature dependence in $S(\Omega)$ persisting up to $\Omega \sim 1$ eV.⁴⁴ That relatively small changes in temperature can induce changes over such a wide range in frequency may be understood as a signature of the delicate balance that strong electronic correlations strike between the potential energy of high-energy states and the kinetic energy of states at lower energies. In the Stoner model of itinerant magnetism, this balance favors a magnetic state in which both the kinetic and potential energies have larger magnitudes than in the nonmagnetic state. We discuss the application of this idea to ruthenium oxides in Sec. IV C.

The relative importance of frequency-dependent quasiparticle scattering, momentum-dependent quasiparticle scattering, and direct excitation of interband transitions in the optical conductivity of transition metal oxides remains poorly understood. The issue has been most actively studied in the copper oxides, for which the emerging picture is that all three of these effects can be important, with some dependence on material and doping level that remains to be clarified.^{9,45,46} Recent photoemission results on a layered manganite reveal momentum and frequency dependence in the quasiparticle scattering rate that strongly resembles that

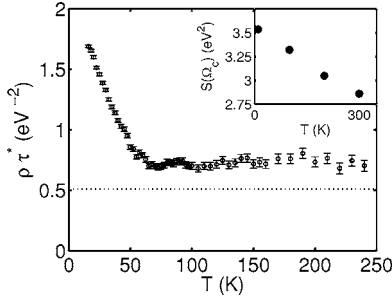


FIG. 4. The product $\rho\tau^*$ as a function of temperature, with the prediction from band theory for the *ab* plane shown as a dotted line. The inset shows the temperature dependence of $S(\Omega_c)$ derived from this work together with data from Lee *et al.* (Ref. 4), with $\Omega_c = 2\pi \times 1500 \text{ cm}^{-1}$.

of the cuprates, indicating that at least some of the phenomenology that has been elaborated for the cuprates can be extended to other perovskite oxides.⁴⁷ However, the layered ruthenate Sr_2RuO_4 has been studied in exquisite detail with transport measurements, and have been successfully interpreted with the assumption that the scattering rate anisotropy is weak;⁴⁸ less is known about other ruthenium oxides.

A more detailed understanding of the material dependence of this variation is urgently needed, and one of the primary lessons of the cuprate literature is that this requires careful and quantitative comparison of results from a variety of experimental techniques on well-characterized samples. For a given set of assumptions our results provide significant experimental constraints on model parameters, and in some cases these are sufficient to exclude entire classes of models: we have seen already in Sec. IV A that our results are poorly characterized by a simple Drude model, and in Sec. IV E we show that the scaling analysis used by Lee *et al.*⁴ encounters fundamental difficulties when applied to our measurements. However, considerable ambiguity remains, particularly regarding the role of momentum dependent scattering, so we provide ample discussion of the origins of this ambiguity and possible ways to clarify it in future work.

C. Temperature dependent spectral weight

Figures 1 and 2 reveal two competing trends in the spectral weight at low frequencies. Setting $\Omega_c = 2\pi \times 1500 \text{ cm}^{-1}$, $S(\Omega_c)$ clearly increases as the temperature is lowered; this is shown in the inset to Fig. 4. At temperatures $T < 100 \text{ K}$, however, a clear peak develops at $\omega = 0$, and this peak becomes sharper as the temperature is lowered. Although we have shown that the frequency dependence of this peak is not described well by Eq. (1) over our entire bandwidth, good fits are obtained over the restricted frequency range $\nu \leq 0.5 \text{ THz}$, and from these we can obtain effective Drude parameters that are valid in the low-frequency limit: these are simply $\omega_p^{*2} = \omega_p^2/[1 + \lambda(0)]$ and $\tau^* = \tau[1 + \lambda(0)]$ in extended Drude parametrization of Eq. (2).⁴⁹ We find that in contrast with $S(\Omega_c)$, the spectral weight associated with this low-energy Drude peak decreases as temperature decreases. Thus, as the conductivity of CaRuO_3 gains spectral weight below Ω_c , presumably from energies well above Ω_c , this

weight is further redistributed within this low frequency bandwidth.

We demonstrate this effect in Fig. 4 by plotting the temperature dependence of $\rho\tau^*$, where ρ is the measured dc resistivity and $1/\tau^*$ is the scattering rate obtained from the fit to Eq. (1) over a restricted frequency range. In the extended Drude model of Eq. (2),

$$\rho\tau^* = \frac{1}{\epsilon_0\omega_p^{*2}} = \frac{1 + \lambda(0)}{\epsilon_0\omega_p^2}, \quad (7)$$

and is therefore a direct measure of optical mass renormalization. The band theory prediction is shown as a dotted line.²¹ At high temperatures the measurement reveals a constant value of $\rho\tau^*$ that is renormalized above the band theory value by 40%. Near $T = 50 \text{ K}$, however, $\rho\tau^*$ increases sharply as temperature is reduced, to reach a value that exceeds three times the band theory prediction. In a Fermi liquid we expect a temperature regime over which renormalization effects are saturated, but over the temperature range studied, we see no indication that this occurs. Similar temperature dependence was observed in $\rho\tau^*$ for SrRuO_3 .^{6,50} Using low-temperature transport measurements as a guide,^{3,51} we expect that ultimately this temperature dependence does saturate at some disorder-dependent crossover scale below $T \sim 10 \text{ K}$ in the SrRuO_3 samples, but may never saturate in CaRuO_3 .

We emphasize the strengths of this experimental approach. One of the primary advantages of THz-TDS is its ability to measure the real and imaginary parts of $\tilde{\sigma}(\omega)$ directly, and from this we determine the low-frequency effective Drude parameters ω_p^* and τ^* with high accuracy. Kramers-Kronig relations imply

$$\tau^* \equiv \frac{1}{\sigma_0} \left. \frac{d\sigma_2}{d\omega} \right|_{\omega \rightarrow 0} = \frac{2}{\pi} \int_0^\infty \frac{1 - [\sigma_1(\omega')/\sigma_0]}{\omega'^2} d\omega', \quad (8)$$

where σ_0 is the dc conductivity, and the subtraction in the numerator is used to remove the singularity at $\omega' = 0$. Thus τ^* is related to an inverse moment of the conductivity spectral weight that extends to infinite frequency, although in practice the integral is dominated by the curvature of $\sigma_1(\omega)$ near $\omega = 0$. Thus the parameters τ^* , ω_p^* determine the low-frequency Taylor expansion of $\tilde{\sigma}(\omega)$ up to second order, independent of any model. Higher-order terms can be obtained by fitting a more complex model to a wider frequency range, so, in principle, our measurements can be analytically continued to outside of our measured bandwidth, up to a range that is determined by the measurement noise.⁵²

The value of τ^* is not easily obtained from infrared reflectance at the lowest frequencies. At zero frequency, the reflectance of any metal is unity, and an expansion near $\omega = 0$ gives

$$R(\omega) \cong 1 - \sqrt{\frac{8\omega\epsilon_0}{\sigma_0}} \left(1 - i \frac{\omega\tau^*}{2} \right). \quad (9)$$

The first correction is the well-known Hagen-Rubens approximation, and the second correction in parentheses displays the sensitivity to τ^* . With $\omega = 2\pi \times 1 \text{ THz}$ and $\sigma_0 = (100 \mu\Omega \text{ cm})^{-1}$, the Hagen-Rubens correction is about 2%

and depends only on the dc conductivity: all information about τ^* is buried in a correction to this correction. Consequently, infrared reflectance measurements of τ^* are much less reliable than transmission-geometry THz-TDS measurements, even when the infrared conductivity extrapolates well to the dc value.

Interpretation of these spectral weight trends is model dependent. Both arise naturally out of the strong scattering rate anisotropy model, whereas in a frequency-dependent scattering picture the two trends would require different origins. With strongly anisotropic scattering $S(\Omega_c)$ increases as temperature is lowered because the Drude contributions to Eq. (4) with $\gamma \sim \Omega_c$ become narrower, shifting spectral weight from the tails above $\omega = \Omega_c$ into the central peak at $\omega = 0$. At the same time, γ_{\min} decreases and causes the singularity near γ_{\min} to get sharper, so that a Drude extrapolation from the low-frequency $\tilde{\sigma}(\omega)$ shrinks in weight even as $S(\Omega_c)$ grows.⁴⁹ In this model, the temperature dependence of $\rho\tau^*$ reflects the distribution $\alpha(\gamma)$. By contrast, in the usual interpretation of the frequency-dependent scattering model, the temperature scale for changes in $\rho\tau^*$ reflects the energy scale of bosonic modes that renormalize the carriers. Here, spectral weight is shifted away from low frequencies as the carriers become more massive, but in the standard electron-phonon picture $S(\Omega_c)$ should remain constant for Ω_c larger than the characteristic frequency of the boson. Temperature dependence in $S(\Omega_c)$ at frequencies higher than any natural low-energy bosonic scale, as observed here and by Lee *et al.*,⁴ is commonly taken to be a sign that strong correlation effects are important.

A peak in the far-infrared near $\nu \sim 200 \text{ cm}^{-1}$ is observed in both CaRuO_3 and SrRuO_3 , and is an obvious candidate for a bosonic mode that could interact with the carriers to produce renormalization. The energy scale is about a factor of six greater than the characteristic temperature scale displayed by Fig. 4, and it grows sharper as the temperature is lowered, in qualitative agreement with a Holstein band assignment.³⁴ Phonons in this energy range have been observed with Raman spectroscopy in both CaRuO_3 and SrRuO_3 , and several of these harden in SrRuO_3 upon entry into the ferromagnetic state.⁵³⁻⁵⁵ However, their positions are virtually temperature independent in CaRuO_3 .⁵³ Also, the position of the peak in the optical conductivity is strongly temperature dependent and merges with the peak at $\omega = 0$ at low temperatures.^{4,32} This is not easy to understand in a conventional electron-boson interaction picture, nor is it consistent with an assignment of the peak to static disorder.^{56,57}

Qualitatively similar behavior has been seen in copper oxides^{9,23} and several authors have argued that this can be understood as direct excitation of nearly critical charge fluctuations that result from proximity to a charge-ordering or “stripe” instability.⁵⁸⁻⁶⁰ Additionally, interband transitions are expected at low energies in the ruthenates, as discussed in Sec. III. Without additional interactions one would not expect these to be strongly temperature-dependent; at low energies, however, quantum orbital fluctuations and interactions with phonons may produce behavior that is not captured by this intuition. The importance of quasiparticle scattering from orbital fluctuations in SrRuO_3 has been

TABLE I. Properties of three-dimensional ruthenates: specific heat renormalization m^*/m_b , plasma frequency renormalization $\omega_{pb}^2/\omega_p^{*2}$, kinetic energy gain ΔK , and the magnetic ground state. Note that BaRuO_3 refers to the four-layer hexagonal compound; CaRuO_3 and SrRuO_3 are both perovskites. To calculate m^*/m_b and $\omega_{pb}^2/\omega_p^{*2}$ band theory values were taken from Mazin and Singh (Ref. 21) and references to experimental data are indicated in the footnotes.

Material	m^*/m_b	$\omega_{pb}^2/\omega_p^{*2}$	ΔK (eV/Ru)	Ground state
SrRuO_3	4 ^a	13 ^b	0.4 ^c	Ferromagnet
CaRuO_3	13 ^a	3.5 ^d	0.2 ^e	Strong paramagnet
BaRuO_3			0.1 ^f	Weak paramagnet

^aReference 29.

^bReferences 6 and 50.

^cReferences 6 and 32.

^dThis work.

^eThis work and Ref. 4.

^fReference 75.

emphasized by Laad and Müller-Hartmann.¹¹

Yet another intriguing possibility is that the far-infrared peak is a precursor to a Mott instability. The transition from ferromagnetism to paramagnetism in the solid-state solution $\text{Ca}_{1-x}\text{Sr}_x\text{RuO}_3$ near $x=0.3$ mirrors a similar transition in $\text{Ca}_{2-x}\text{Sr}_x\text{RuO}_4$ near $x=0.5$, and the end member Ca_2RuO_4 is a Mott insulator with an optical gap of 0.2 eV.⁶¹⁻⁶⁶ Also, the spin fluctuation spectrum of the ruthenium oxides typically has strong antiferromagnetic fluctuations that are associated with Fermi surface nesting.²⁴ A variety of theoretical methods indicate that the Mott transition occurs inhomogeneously over the Fermi surface and that this is preceded on the metallic side by large momentum-dependence the single-particle scattering rate.⁶⁷⁻⁷⁰ In these models, a Mott-induced pseudogap appears in the optical conductivity as portions of the Fermi surface become gapped and we would then identify the frequency scale of this pseudogap with the partial gap on the Fermi surface. However, pseudogaps in other systems near a Mott transition do not generally show such strong temperature dependence⁷¹ and the room temperature optical conductivity of metallic samples of $\text{Ca}_{2-x}\text{Sr}_x\text{RuO}_4$ does not reveal a far-infrared peak.⁷² It would be very interesting to examine the variation of the far-infrared properties with temperature in this layered system.

In Table I we organize some of the trends across three-dimensional ruthenate compounds that reveal a striking correlation between magnetism and spectral weight.³¹ The spectral weight is written here as a kinetic energy using Eq. (6) and clearly increases as the tendency toward ferromagnetism becomes stronger. Itinerant magnetism results from a competition between the kinetic energy of the itinerant carriers and the exchange-correlation energy associated with their interactions, with interactions favoring magnetism.^{73,74} Density functional theory calculations give an energy difference of 0.18 eV/Ru between magnetic and nonmagnetic states of SrRuO_3 ; the kinetic energy should increase by more than this in the magnetic state, because the total energy includes a negative exchange-correlation contribution. This is consistent with the tabulated values of ΔK . Only ferromagnetic

SrRuO₃ exhibits enough kinetic energy change to generate the magnetic energy reduction expected from band theory, whereas nearly ferromagnetic CaRuO₃ is at the borderline and weakly paramagnetic BaRuO₃ falls well short of it.

The behavior of m^*/m_b determined from specific heat shows stronger renormalization for CaRuO₃ than for SrRuO₃ but with $\omega_{pb}^2/\omega_p^{*2}$ this trend is reversed. Where data is available for other materials these two measures of carrier renormalization are usually consistent to within a factor of 2,⁵ so this discrepancy is problematic. Even more troubling is the observation that $\omega_{pb}^2/\omega_p^{*2} > m^*/m_b$ for SrRuO₃: in Fermi liquid theory, the current renormalization measured by $\omega_{pb}^2/\omega_p^{*2}$ is typically lower than the velocity renormalization measured by m^*/m_b .

These ratios are defined with reference to a band structure calculation that gives 13 eV² for ω_{pb}^2 in SrRuO₃ and 2 eV² for the *ab* plane of CaRuO₃.²¹ This is actually the dominant source of variation in $\omega_{pb}^2/\omega_p^{*2}$ between the two materials. The quantity ω_{pb}^2 is an excited-state property determined from a Fermi-surface average of v_F^2 , so it is possible that these anomalies reflect systematic uncertainties in the DFT calculation. Alternatively, the independence of $\omega_{pb}^2/\omega_p^{*2}$ and m^*/m_b noted here may be a sign that the sharpness of $\sigma_1(\omega)$ near $\omega=0$ is not simply related to carrier renormalization, and that other effects such as momentum dependence must be considered. A more systematic investigation of these issues would be very desirable.

D. Multicomponent parametrization and the anomalous power law

In this section we provide a more detailed discussion of the functional form of $\tilde{\sigma}(\omega, T)$. As we have described in Sec. IV A, a simple Drude model is inadequate to describe our measurements, especially at low temperatures. However, as we have discussed in Sec. IV B, once a simple Drude model is excluded by the data there are several options for further analysis, each with its own set of implicit physical assumptions. Our goal in this section is to be empirical as possible, while drawing attention to physical interpretations where appropriate.

As a first step we attempt to model our results with the anomalous power law expression given in Eq. (3). This form provided a successful extrapolation of THz-TDS measurements on SrRuO₃, out to frequencies nearly 100 times the upper measurement bandwidth,⁶ further support for it has come from work on MnSi and optimally doped cuprate superconductors.^{7,8,10} On the other hand, extrapolations to zero frequency with SrRuO₃ appear problematic,^{3,51} and it is impossible for Eq. (3) to reproduce the conductivity peak that exists near $\nu \sim 200$ cm⁻¹ in both CaRuO₃ and SrRuO₃ for $T \geq 100$ K. We show the best fit of Eq. (3) to THz-TDS data at $T=16$ K as long dashed lines in Figs. 1 and 2.

While the fit is better at high frequencies than the Drude model, important differences remain. Above $\nu \sim 0.5$ THz, Eq. (3) lies significantly above the measured $\sigma_2(\omega)$ shown in Fig. 1; this disagreement persists up to room temperature, where the power-law model, such as the Drude model, cannot reproduce the negative values exhibited by the measure-

ments. As with the Drude model, the discrepancy in $\sigma_2(\omega)$ indicates that the power-law model underestimates $\sigma_1(\omega)$ at higher frequencies. We emphasize that by referring to THz-TDS measurements of $\sigma_2(\omega)$, we do not need to rely on IR measurements to reach this conclusion; however, they do support it. The extrapolated THz-TDS measurements sit well beneath $\sigma_1(\omega)$ shown in Fig. 2, over the entire IR bandwidth. If we assume that the theoretically expected anisotropy becomes evident at low temperatures, the discrepancy is near the limit of the systematic uncertainties discussed in Sec. II. Although it is possible that polarized infrared measurements on similar samples would yield much better agreement, this is unlikely.

We can account for the excess $\sigma_1(\omega)$ at high frequencies and the peak at $\nu \sim 200$ cm⁻¹ by adding a single finite-frequency Lorentzian to Eq. (3), but there are fundamental problems with this approach. Any Lorentzian that we might choose to model the conductivity peak will have a very large overlap integral with the high-frequency tail of Eq. (3), such that the Lorentzian parameters become correlated with the exponent β . The correlation is so strong that the model parameters lose their identifiability: equally good fits to a combination of our data and that of Lee *et al.*⁴ can be obtained with a wide range of values for β , simply by allowing the Lorentzian parameters to change in response.

This is a problem with the mathematical structure of the fitting equations, so any gains from improving the measurement accuracy will have limited value. To appreciate this, recall that an underdamped Lorentzian may be expressed in a partial fraction expansion as the difference between two Drude peaks:

$$\frac{\omega}{\Gamma\omega + i(\omega_0^2 - \omega^2)} = \frac{A_+}{\gamma_+ - i\omega} - \frac{A_-}{\gamma_- - i\omega}, \quad (10)$$

where $\gamma_{\pm} = (\Gamma \pm \sqrt{\Gamma^2 - 4\omega_0^2})/2$ and $A_{\pm} = \gamma_{\pm}/(\gamma_+ - \gamma_-)$. Adding this to the conductivity influences the anomalous power law model by modifying the distribution of carrier lifetimes $\alpha(\gamma)$ in Eq. (4). Although the modification is limited to two discrete values $\gamma = \gamma_{\pm}$, this discreteness is virtually eliminated from $\tilde{\sigma}(\omega)$ by the smoothing effect of the integral kernel in Eq. (4). Moreover, the smoothing operation induces changes in $\tilde{\sigma}(\omega)$ that are difficult to distinguish from changes in β .

These considerations suggest that instead of using our data to test the validity of the anomalous power law model of Eq. (3), it is more useful to examine the constraints that our measurements place on $\alpha(\gamma)$ in Eq. (4). To make progress toward this goal, however, we must first recognize that inversion of this integral equation is an ill-posed problem, in the sense that small changes in $\tilde{\sigma}(\omega)$ can produce wildly varying changes in $\alpha(\gamma)$.⁷⁶ To address this issue we discretize the integral into a sum over a finite set of terms.

We express the conductivity as a sum of free and bound carriers, $\tilde{\sigma} = \tilde{\sigma}_f + \tilde{\sigma}_b$, and describe the free carriers by a sum over Drude peaks with different amplitudes A_k and scattering rates γ_k :

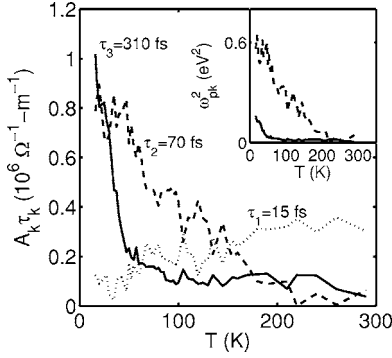


FIG. 5. Temperature dependence of the fitted amplitudes for the three Drude terms. The fits use temperature independent relaxation times with $\tau_1=310$, $\tau_2=70$ and $\tau_3=15$ fs, as labeled in the plot. The same line styles are used in the inset, showing the spectral weights associated with the two narrowest Drude terms.

$$\bar{\sigma}_f(\omega) = \sum_{k=1}^N \frac{A_k}{\gamma_k - i\omega}. \quad (11)$$

The amplitudes A_k may be understood as a kind of low-resolution image of $\alpha(\gamma)$: as long as the parameters γ_k are well separated and cover a range over which $\alpha(\gamma)$ is relatively large, the associated A_k will serve as proxies for the strength of $\alpha(\gamma)$ in the vicinity of γ_k . We find that to achieve this it is effective to hold the γ_k fixed globally at equal logarithmic spacing, allow the range $\gamma_N - \gamma_1$ to vary, and increase N until all temperatures are fit well. The resulting model is linear in the parameters and consequently more stable than if all of the parameters are free.⁷⁷ This procedure is capable of reproducing Eq. (3) for relatively small N ; the precise value depends on the frequency range and the signal to noise ratio. In simulations we have found that if we add Gaussian noise with amplitude $\sigma=10^{-3}$ to Eq. (3) with $\beta=1/2$ and a frequency interval $\omega \in (0.3/\tau, 30/\tau)$, then a fit with Eq. (11) and $N=4$ is enough to achieve a normalized chi-squared of $\chi^2/\nu \cong 1$.

We model the bound carriers as a single finite-frequency Lorentzian $\tilde{\sigma}_b = \omega A_L / [\gamma_L \omega - i(\omega^2 - \omega_0^2)]$. The parameter identification problem encountered when a Lorentzian was added to Eq. (3) is not eliminated in fits to the discrete Drude sum, but for terms in Eq. (11) that have γ_k comparable to or less than the THz-TDS frequency band, the resulting systematic error in the parameters will be small. For all temperatures we augment our THz-TDS data with published infrared reflectance measurements from above 500 cm^{-1} , for which $\sigma_1(\omega)$ is nearly temperature independent.⁴ At intermediate frequencies not included in our fits, where the infrared data of Lee *et al.*⁴ varies over the four measured temperatures, a discrepancy not greater than 30% appears between the measurements and the model; this is also true of fits to Eq. (3) plus a Lorentzian.

We find that $N=3$ is sufficient to achieve good fit, a clear deviation from simple Drude dynamics. The scattering times that we obtain are $\tau_k=1/\gamma_k$ of 310, 70, and 15 fs, corresponding to $\gamma_k=0.5, 2.3,$ and 10.6 THz , respectively. With the THz-TDS band limit of 1.25 THz , the first two ampli-

tudes are specified most accurately. Figure 5 shows the best-fit temperature-dependent amplitudes $A_k(T)$, scaled by their associated scattering time to allow direct comparison with the conductivity. The $\tilde{\sigma}(\omega)$ obtained from fits at selected temperatures are shown in Fig. 1 as solid lines. We have verified that at all temperatures $\sum_k A_k(T) \tau_k(T) = \sigma_{dc}(T) \pm 5\%$ for consistency. The statistical uncertainty in $A_k \tau_k$ is represented accurately by the temperature-dependent fluctuations, with r.m.s. amplitudes of about $5 \times 10^4 \Omega^{-1} \text{ m}^{-1}$. These fluctuations are correlated at any given temperature, particularly those between A_2 and A_3 , as a consequence of the nonorthogonality of the basis functions in Eq. (11). We have estimated the correlation matrix from the curvature of the χ^2 function, and at each temperature $\rho_{ij} \geq 0.6$ for $i \neq j$. One consequence of this correlation is that the confidence region in the A_k parameter space is much smaller than the fluctuations in Fig. 5 would suggest. This is supported by the relatively small rms residuals for the fits in Fig. 1. The parameters A_L , γ_L and ω_0 are also correlated with the A_k ; this is strongest among A_L , A_1 and A_2 .

The inset of Fig. 5 shows the spectral weights, as measured by $\omega_{pk}^2 = A_k \gamma_k / \epsilon_0$, associated with the two narrowest Drude terms. The sum of all three terms is relatively temperature independent and yields $\omega_{pT}^2 \cong 1 \text{ eV}^2$; we consider this as an upper bound on the free-carrier conductivity described by Eq. (11), with $\omega_{p1}^2 \cong 0.15 \text{ eV}^2$ providing a lower bound. For all temperatures, the Lorentzian term is heavily overdamped, with weakly temperature-dependent parameters near $\omega_0 \sim 300 \text{ cm}^{-1}$, $\gamma_L \sim 3000 \text{ cm}^{-1}$, and $A_L/\gamma_L \sim 3 \times 10^5 \Omega^{-1} \text{ cm}^{-1}$. This gives a plasma frequency for the bound carriers of $\Omega_{pL} = 2.5 \text{ eV}$, yielding a total spectral weight $\sum_k \omega_{pk}^2 + \Omega_{pL}^2 \cong 7.25 \text{ eV}^2$, much larger than the free carrier contribution. Band theory predicts $\omega_p^2 \cong 2 \text{ eV}^2$, much closer to the free carrier estimate obtained here.²¹

We can now connect these observations with those of Sec. IV C and to possible future experiments. The rise of the narrowest Drude amplitude A_3 near $T=50 \text{ K}$ coincides with the sharp upturn in $\rho\tau^*$ shown in Fig. 4, and establishes that the temperature dependence in $\rho\tau^*$ is linked to the appearance of a new time scale of order 300 fs. From optical measurements alone, it is impossible to tell whether this time scale is associated with quasiparticles everywhere on the Fermi surface or only with those at particular ‘‘cold spots.’’ The implied scattering rate of 2 meV should give well-defined peaks in other spectroscopies such as tunneling and photoemission, and it would be interesting to search for these and compare with the results described here.

The growth of the two narrowest Drude peaks with $\tau_2=70 \text{ fs}$ and $\tau_3=310 \text{ fs}$ can account completely for the spectral weight gain shown in the inset of Fig. 4. The energy scale at which the sum rule is restored is currently unclear, and it would be instructive to do careful measurements at higher frequencies to determine this. In an anisotropic scattering model, gains at low frequencies should come from the tails of broader Drude terms, whereas models that rely on strong correlations for spectral weight transfer would generally predict that it is drawn from excitations at higher energies that are more well defined.

In principle, the temperature dependence of all three Drude amplitudes could provide evidence for or against the

anomalous power law model of Eq. (3). If we limit our attention to the THz-TDS measurements and exclude higher frequencies, then the anomalous power law with $\beta \equiv 1/2$ does characterize the basic variation of the data with frequency, with small but significant discrepancies becoming noticeable in $\sigma_2(\omega)$ at higher frequencies. If we wish to explain the behavior of $\tilde{\sigma}(\omega)$ from dc up to the mid-IR, however, then in practice we have found that the strongest inference that we can draw is that there is a distribution of time scales that spans 15–310 fs, and that the two narrowest Drude peaks in the fit are depleted with increasing temperature as shown in Fig. 5.

Quantitative comparisons with specific models for the distribution are difficult because the kernel of Eq. (4) projects large variations in $\alpha(\gamma)$ onto relatively small variations in $\tilde{\sigma}(\omega)$; they are not impossible, however, and with greater precision over a broader range in frequencies it may be possible to discriminate between the distribution for Eq. (3) and alternatives. We believe that the methodology we have described in this section provides a way to define this experimental challenge more precisely. It may also prove useful for analyzing other examples of anomalous dynamics that have appeared in the terahertz literature; these are commonly fit with functions such as Eq. (3).^{78,79}

Although the model presented in Sec. IV D has several free parameters, it is possible to reduce them further by examining their correlations. In the formulation of Eq. (4) this is because the frequency and temperature dependence of $\tilde{\sigma}(\omega, T)$ are related through the temperature dependence of $\alpha(\gamma)$. To take a simple example, in a Drude model with $\alpha(\gamma) = \delta(\gamma - \kappa T)$, the conductivity is just $\sigma_0 / (1 - i\omega / \kappa T)$ and depends only on the ratio of the two independent variables ω and T . We pursue this idea further in the next section.

E. Scaling analysis

Lee *et al.*⁴ argued that the infrared conductivity of both CaRuO₃ and SrRuO₃ is consistent with the quantum critical scaling relationship given by

$$\tilde{\sigma}(\omega, T) = \omega^\mu f(\omega/T). \quad (12)$$

Figure 6 shows their results for CaRuO₃ at three temperatures, together with our raw THz-TDS data for $T \leq 45$ K. The collapse of the THz-TDS data in Fig. 6 clearly suggests that the conductivity satisfies the scaling hypothesis embodied in Eq. (12), but further analysis shows that this results from a fortuitous correlation of the frequency and temperature dependence over the measurement range and should not be taken as evidence for quantum critical scaling in CaRuO₃. We discuss this conclusion in more detail below, but it is not surprising. While scaling plots such as these are useful for establishing basic phenomenology, it has long been known that they are unreliable for testing the scaling hypothesis itself, because systematic deviations from the scaling law can be difficult to distinguish visually from random noise. For example, in experimental studies of the quantum Hall-insulator transition, $\rho(T)$ measurements that appeared to ex-

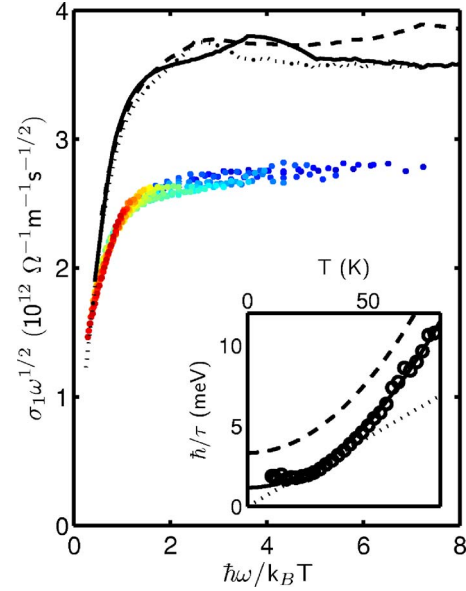


FIG. 6. (Color online) Scaling plots of the raw THz-TDS data (points) for $\omega = 0.25\text{--}0.90$ THz and $T = 6\text{--}45$ K, together with earlier infrared measurements at $T = 10$ (dashed), 100 (dotted) and 200 K (solid) (Ref. 4). The inset shows $\hbar/\tau(T)$ obtained from fits to an anomalous power law with $\beta = 1/2$ (open circles), together with a fit to quadratic temperature dependence (solid) and the line $\hbar/\tau = k_B T$ (dotted). The apparent collapse of the THz-TDS data in the scaling plot results from the approximate overlap of these two distinct functions for $T < 45$ K. The dashed line shows $\hbar/\tau(T)$ obtained from earlier power-law fits for SrRuO₃, with $\beta = 0.4$ (Ref. 6).

hibit tight correlation in a scaling plot were later shown to be fit better by a phenomenological form that manifestly violates the scaling hypothesis.^{80,81} Our analysis follows similar reasoning.

Although the IR and THz-TDS data sets separately appear to overlap well, they clearly do not overlap with each other. As we have discussed in Sec. II it is possible that the mismatch results from sample and measurement differences; however, given the agreement shown in Fig. 2 at high temperatures, this explanation appears unlikely. Moreover, we really should not expect these two data sets to be related at all through a scaling law, even though they appear to have similar behavior in the scaling plot: the THz-TDS measurements cover the narrow peak centered at $\omega = 0$, whereas the IR measurements cover the peak at finite frequency. The main reason for the similarity is the approximate $\sigma_1 \propto 1/\sqrt{\omega}$ high-frequency behavior that causes $\sigma_1 \omega^{1/2}$ to be relatively flat at high frequencies but with different levels. At low frequencies this dependence is cut off in both data sets, by elastic scattering for the THz-TDS measurements and by the 200 cm^{-1} peak in the IR measurements, and it is the approximately linear temperature dependence of both cutoff frequencies that is captured by the scaling plot.

The THz-TDS data shown in Fig. 6 is concentrated at low temperatures and frequencies, where the anomalous power law of Eq. (3) describes $\tilde{\sigma}(\omega)$ reasonably well; the inaccuracies that required additional modeling appear primarily at higher frequencies and temperatures. In this case, it is ac-

ceptable to rely on anomalous power law fits to represent the measurements; this allows us to reduce all of the frequency dependence in $\tilde{\sigma}(\omega, T)$ to a single temperature-dependent parameter $\tau(T)$. Then, if ω/T scaling applies, we expect $1/\tau(T) \propto T$. In the inset to Fig. 6 we show $\hbar/\tau(T)$ for CaRuO_3 , obtained from anomalous power law fits with $\beta = 1/2$. The linear temperature dependence associated with quantum critical scaling is shown as a dotted line, and the results clearly disagree: the dependence is not linear, but quadratic with temperature, although the linear relationship lies close to the quadratic curve over a fairly wide range.

A similar quadratic temperature dependence was observed in THz-TDS measurements on SrRuO_3 .⁶ A fit of the expression

$$\frac{\hbar}{\tau(T)} = \frac{\hbar}{\tau_0} + \frac{k_B T^2}{T_0} \quad (13)$$

to these measurements with $\beta=0.4$ gave $\hbar/\tau_0=3.3$ meV and $T_0=40$ K; this function is shown in the inset for comparison. Fitting Eq. (13) to the CaRuO_3 data with $\beta=0.5$ gives $\hbar/\tau_0=1.2$ meV and $T_0=53$ K, shown also in the inset. The residual term \hbar/τ_0 is a factor of three lower in CaRuO_3 than in SrRuO_3 , but the residual resistivity of the CaRuO_3 and SrRuO_3 samples is comparable. Consequently this variation does not simply reflect a difference in disorder, but is more likely related to a difference in the average carrier velocity, either from the bare band structure or from interactions. The value of T_0 is strikingly similar in these two materials, indicating a common origin that remains poorly understood. This temperature scale has appeared throughout the analysis of this work in different guises, but empirically it signals the onset of a new, surprisingly long time scale in the quasiparticle dynamics.

It would be interesting to see similar analysis done for other materials that have been discussed in terms of quantum critical phenomena. For example, recent work by van der Marel *et al.*⁸ has shown that $\tilde{\sigma}(\omega, T)$ in an optimally doped cuprate superconductor collapses in a scaling plot similar to that shown in Fig. 6. They interpreted this as evidence for an underlying quantum critical point, and discussed several other features in the conductivity that further supported this interpretation. However, their analysis yields a negative critical exponent μ in Eq. (12), and Phillips and Chamon⁸² have argued that this renders the scaling interpretation internally inconsistent; note that the scaling analysis for CaRuO_3 gives $\mu=-1/2$ so a similar exponent problem appears here. Norman and Chubukov⁸³ have argued that an alternative interpretation explains the data equally well. This is unsurprising in light of our analysis: as we have noted, model-dependent details in $\alpha(\gamma)$ are transmitted to $\tilde{\sigma}(\omega)$ with considerable loss of information, so we should expect a va-

riety of physically distinct models to produce qualitatively similar behavior. We have presented a way to pursue further quantitative comparison with theory, by examining $1/\tau(T)$ in a fit of Eq. (3) to the data. Our analysis shows that this simple test of the ω/T scaling hypothesis can be more discriminating than a scaling plot.

V. CONCLUSIONS

In summary, we have used THz-TDS to determine the carrier dynamics of CaRuO_3 at frequencies well below the band covered by infrared spectroscopy. This allows us to resolve a narrow conductivity peak at $\omega=0$ that we have argued is correlated with magnetism and is characterized by multiple time scales. In presenting our results we have emphasized the distribution of scattering rates $\alpha(\gamma)$ that describes our data, and developed analysis methods to characterize it. This distribution may originate from Fermi surface anisotropy, or dynamical considerations or both, and is related to the conductivity through an integral transform that is impossible to invert in the presence of noise. Nonetheless we have shown that the high accuracy and precision that can be obtained with THz-TDS measurements can constrain possibilities and provide guidance for further comparison between experiment and theory.

At the lowest temperatures the maximum time scale approaches nearly a third of a picosecond, much longer than expected from the calculated band structure and measured resistivity. The temperature dependence of $\rho\tau^*$ signals the appearance of this long time scale near $T \sim 50$ K, and we have suggested that this scale may be connected to the far-IR conductivity peak observed by Lee *et al.*⁴ Our data is not well described by a single Drude peak, nor is it described well by a functional form that exhibits ω/T scaling. Clear correlations exist among the amplitudes A_k associated with different scattering rates, and at low frequencies and temperatures this is captured by the anomalous power law form of Eq. (3) with an effective scattering rate given by Eq. (13). In contrast with SrRuO_3 , however, the utility of the anomalous power law description appears to be limited to a fairly restricted domain.

ACKNOWLEDGMENTS

J.S.D. acknowledges support from NSERC, the CIAR Program in Quantum Materials, the Sloan Foundation, and the Research Corporation; he also thanks D. M. Broun, J. Carbotte, T. P. Devereaux, I. Herbut, M. P. Kennett, Y. S. Lee, I. I. Mazin, A. J. Millis, and T. W. Noh for helpful discussions. C.B.E. acknowledges support from National Science Foundation under Grant No. ECS-0210449 and the David and Lucile Packard Foundation.

- ¹R. J. Cava, *Dalton Trans.* **19**, 2979 (2004).
- ²L. Klein, L. Antognazza, T. H. Geballe, M. R. Beasley, and A. Kapitulnik, *Phys. Rev. B* **60**, 1448 (1999).
- ³L. Capogna, A. P. Mackenzie, R. S. Perry, S. A. Grigera, L. M. Galvin, P. Raychaudhuri, A. J. Schofield, C. S. Alexander, G. Cao, S. R. Julian, and Y. Maeno, *Phys. Rev. Lett.* **88**, 076602 (2002).
- ⁴Y. S. Lee, J. Yu, J. S. Lee, T. W. Noh, T. H. Gimm, H.-Y. Choi, and C. B. Eom, *Phys. Rev. B* **66**, 041104(R) (2002).
- ⁵A. J. Millis, in *Strong Interactions in Low Dimensions*, edited by D. Baeriswyl and L. Degiorgi (Kluwer, Netherlands, 2004), pp. 195–235.
- ⁶J. S. Dodge, C. P. Weber, J. Corson, J. Orenstein, Z. Schlesinger, J. W. Reiner, and M. R. Beasley, *Phys. Rev. Lett.* **85**, 4932 (2000).
- ⁷F. P. Mena, D. van der Marel, A. Damascelli, M. F ath, A. A. Menovsky, and J. A. Mydosh, *Phys. Rev. B* **67**, 241101(R) (2003).
- ⁸D. van der Marel, H. J. A. Moegraaf, J. Zaanen, Z. Nussinov, F. Carbone, A. Damascelli, H. Eisaki, M. Greven, P. Kes, and M. Li, *Nature (London)* **425**, 271 (2003).
- ⁹D. N. Basov and T. Timusk, *Rev. Mod. Phys.* **77**, 721 (2005).
- ¹⁰L. B. Ioffe and A. J. Millis, *Phys. Rev. B* **58**, 11631 (1998).
- ¹¹M. S. Laad and E. M uller-Hartmann, *Phys. Rev. Lett.* **87**, 246402 (2001).
- ¹²M. C. Nuss and J. Orenstein, in *Millimeter and Submillimeter Wave Spectroscopy of Solids*, edited by G. Gr uner (Springer-Verlag, Berlin, 1998), pp. 7–50.
- ¹³C. B. Eom, J. Z. Sun, K. Yamamoto, A. F. Marshall, K. E. Luther, T. H. Geballe, and S. S. Laderman, *Appl. Phys. Lett.* **55**, 595 (1989).
- ¹⁴C. B. Eom, R. J. Cava, R. M. Fleming, J. M. Phillips, R. B. van Dover, J. H. Marshall, J. W. P. Hsu, J. J. Krajewski, and J. W. F. Peck, *Science* **258**, 1766 (1992).
- ¹⁵R. A. Rao, Q. Gan, C. B. Eom, R. J. Cava, Y. Suzuki, J. J. Krajewski, S. C. Guasepohl, and M. Lee, *Appl. Phys. Lett.* **70**, 3035 (1997).
- ¹⁶Q. Gan, R. A. Rao, and C. B. Eom, *Appl. Phys. Lett.* **70**, 1962 (1997).
- ¹⁷J.-P. Maria, H. L. McKinstry, and S. Trolier-McKinstry, *Appl. Phys. Lett.* **76**, 3382 (2000).
- ¹⁸A. F. Santander-Syro, R. P. S. M. Lobo, N. Bontemps, Z. Konstantinovic, Z. Z. Li, and H. Raffy, *Phys. Rev. Lett.* **88**, 097005 (2002).
- ¹⁹A. F. Santander-Syro, R. P. S. M. Lobo, N. Bontemps, W. Lopera, D. Girata, Z. Konstantinovic, Z. Z. Li, and H. Raffy, *Phys. Rev. B* **70**, 134504 (2004).
- ²⁰M. Schultz, L. Klein, J. W. Reiner, and M. R. Beasley, *Phys. Rev. B* **73**, 085109 (2006).
- ²¹I. I. Mazin and D. J. Singh, *Phys. Rev. B* **56**, 2556 (1997); **73**, 189903(E) (2006).
- ²²Y. S. Lee (private communication).
- ²³S. Lupi, P. Calvani, M. Capizzi, and P. Roy, *Phys. Rev. B* **62**, 12418 (2000).
- ²⁴D. J. Singh and I. I. Mazin, in *Ruthenate and Rutheno-Cuprate Materials*, edited by C. Noce, A. Vecchione, M. Cuoco, and A. Romano, *Lecture Notes in Physics* (Springer, Berlin, 2002), pp. 256–70.
- ²⁵A. Callaghan, C. W. Moeller, and R. Ward, *Inorg. Chem.* **5**, 1572 (1966).
- ²⁶K. Yoshimura, T. Imai, T. Kiyama, K. R. Thurber, A. W. Hunt, and K. Kosuge, *Phys. Rev. Lett.* **83**, 4397 (1999).
- ²⁷T. He and R. J. Cava, *Phys. Rev. B* **63**, 172403 (2001).
- ²⁸T. He and R. J. Cava, *J. Phys.: Condens. Matter* **13**, 8347 (2001).
- ²⁹M. Shepard, S. McCall, G. Cao, and J. E. Crow, *J. Appl. Phys.* **81**, 4978 (1997).
- ³⁰L. Degiorgi, *Rev. Mod. Phys.* **71**, 687 (1999).
- ³¹M. Quijada, J.  erne, J. R. Simpson, H. D. Drew, K. H. Ahn, A. J. Millis, R. Shreekala, R. Ramesh, M. Rajeswari, and T. Venkatesan, *Phys. Rev. B* **58**, 16093 (1998).
- ³²P. Kostic, Y. Okada, N. C. Collins, Z. Schlesinger, J. W. Reiner, L. Klein, A. Kapitulnik, T. H. Geballe, and M. R. Beasley, *Phys. Rev. Lett.* **81**, 2498 (1998).
- ³³J. S. Lee, Y. S. Lee, T. W. Noh, K. Char, J. Park, S.-J. Oh, J.-H. Park, C. B. Eom, T. Takeda, and R. Kanno, *Phys. Rev. B* **64**, 245107 (2001).
- ³⁴A. V. Puchkov, D. N. Basov, and T. Timusk, *J. Phys.: Condens. Matter* **8**, 10049 (1996).
- ³⁵P. B. Allen, *Phys. Rev. B* **3**, 305 (1971).
- ³⁶W. G tze and P. W lfle, *Phys. Rev. B* **6**, 1226 (1972).
- ³⁷P. B. Allen, cond-mat/0407777 (unpublished).
- ³⁸M. A. Gilmore, S. Kamal, D. M. Broun, and J. S. Dodge, *Appl. Phys. Lett.* **88**, 141910 (2006).
- ³⁹D. N. Lynch, R. Rosei, and J. H. Weaver, *Solid State Commun.* **9**, 2195 (1971).
- ⁴⁰C. S. Wang and J. Callaway, *Phys. Rev. B* **9**, 4897 (1974).
- ⁴¹M. J. Rozenberg, G. Kotliar, H. Kajueter, G. A. Thomas, D. H. Rapkine, J. M. Honig, and P. Metcalf, *Phys. Rev. Lett.* **75**, 105 (1995).
- ⁴²A. Georges, G. Kotliar, W. Krauth, and M. J. Rozenberg, *Rev. Mod. Phys.* **68**, 13 (1996).
- ⁴³D. M. Broun (private communication).
- ⁴⁴M. Ortolani, P. Calvani, and S. Lupi, *Phys. Rev. Lett.* **94**, 067002 (2005).
- ⁴⁵N. E. Hussey, J. R. Cooper, J. M. Wheatley, I. R. Fisher, A. Carrington, A. P. Mackenzie, C. T. Lin, and O. Milat, *Phys. Rev. Lett.* **76**, 122 (1996).
- ⁴⁶Y. S. Lee, K. Segawa, Z. Q. Li, W. J. Padilla, M. Dumm, S. V. Dordevic, C. C. Homes, Y. Ando, and D. N. Basov, *Phys. Rev. B* **72**, 054529 (2005).
- ⁴⁷N. Mannella, W. L. Yang, X. J. Zhou, H. Zheng, J. F. Mitchell, J. Zaanen, T. P. Devereaux, N. Nagaosa, Z. Hussain, and Z. X. Shen, *Nature (London)* **438**, 474 (2005).
- ⁴⁸C. Bergemann, A. P. Mackenzie, S. R. Julian, D. Forsythe, and E. Ohmichi, *Adv. Phys.* **52**, 639 (2003).
- ⁴⁹D. van der Marel, *Phys. Rev. B* **60**, R765 (1999).
- ⁵⁰J. S. Dodge, J. Corson, R. Mallozzi, J. Orenstein, J. Reiner, and M. R. Beasley, *QELS Technical Digest* (1999), p. 212.
- ⁵¹Y. Kats and L. Klein, *Physica B* **312-3**, 793 (2002).
- ⁵²R. Hulth en, *J. Opt. Soc. Am.* **72**, 794 (1982).
- ⁵³N. Kolev, C. L. Chen, M. Gospodinov, R. P. Bontchev, V. N. Popov, A. P. Litvinchuk, M. V. Abrashev, V. G. Hadjiev, and M. N. Iliev, *Phys. Rev. B* **66**, 014101 (2002).
- ⁵⁴M. N. Iliev, A. P. Litvinchuk, H.-G. Lee, C. L. Chen, M. L. Dezaneti, C. W. Chu, V. G. Ivanov, M. V. Abrashev, and V. N. Popov, *Phys. Rev. B* **59**, 364 (1999).
- ⁵⁵D. Kirillov, Y. Suzuki, L. Antognazza, K. Char, I. Bozovic, and T. H. Geballe, *Phys. Rev. B* **51**, 12825 (1995).
- ⁵⁶D. N. Basov, B. Dabrowski, and T. Timusk, *Phys. Rev. Lett.* **81**, 2132 (1998).

- ⁵⁷R. P. S. M. Lobo, E. Y. Sherman, D. Racah, Y. Dagan, and N. Bontemps, *Phys. Rev. B* **65**, 104509 (2002).
- ⁵⁸S. Caprara, C. Di Castro, S. Fratini, and M. Grilli, *Phys. Rev. Lett.* **88**, 147001 (2002).
- ⁵⁹A. Lucarelli *et al.*, *Phys. Rev. Lett.* **90**, 037002 (2003).
- ⁶⁰M. Dumm, S. Komiya, Y. Ando, and D. N. Basov, *Phys. Rev. Lett.* **91**, 077004 (2003).
- ⁶¹A. Kanbayasi, *J. Phys. Soc. Jpn.* **44**, 108 (1978).
- ⁶²L. Mieville, T. H. Geballe, L. Antognazza, and K. Char, *Appl. Phys. Lett.* **70**, 126 (1997).
- ⁶³P. Khalifah, I. Ohkubo, H. M. Christen, and D. G. Mandrus, *Phys. Rev. B* **70**, 134426 (2004).
- ⁶⁴S. Nakatsuji and Y. Maeno, *Phys. Rev. Lett.* **84**, 2666 (2000).
- ⁶⁵S. Nakatsuji and Y. Maeno, *Phys. Rev. B* **62**, 6458 (2000).
- ⁶⁶A. V. Puchkov, M. C. Schabel, D. N. Basov, T. Startseva, G. Cao, T. Timusk, and Z.-X. Shen, *Phys. Rev. Lett.* **81**, 2747 (1998).
- ⁶⁷T. A. Maier, T. Pruschke, and M. Jarrell, *Phys. Rev. B* **66**, 075102 (2002).
- ⁶⁸C. Kusko, R. S. Markiewicz, M. Lindroos, and A. Bansil, *Phys. Rev. B* **66**, 140513(R) (2002).
- ⁶⁹D. Sénéchal and A.-M. S. Tremblay, *Phys. Rev. Lett.* **92**, 126401 (2004).
- ⁷⁰O. Parcollet, G. Biroli, and G. Kotliar, *Phys. Rev. Lett.* **92**, 226402 (2004).
- ⁷¹M. Imada, A. Fujimori, and Y. Tokura, *Rev. Mod. Phys.* **70**, 1039 (1998).
- ⁷²J. S. Lee, S. J. Moon, T. W. Noh, S. Nakatsuji, and Y. Maeno, *Phys. Rev. Lett.* **96**, 057401 (2006).
- ⁷³C. Herring, in *Magnetism*, edited by G. T. Rado and H. Suhl (Academic Press, New York, 1966), Vol. IV.
- ⁷⁴J. Kübler, *Theory of Itinerant Electron Magnetism* (Oxford University Press, Oxford, 2000).
- ⁷⁵Y. S. Lee, J. S. Lee, K. W. Kim, T. W. Noh, J. Yu, Y. Bang, M. K. Lee, and C. B. Eom, *Phys. Rev. B* **64**, 165109 (2001).
- ⁷⁶A. N. Tikhonov and V. Y. Arsenin, *Solutions of Ill-posed Problems* (Halsted Press, Washington, 1977).
- ⁷⁷C. Lanczos, *Applied Analysis* (Prentice-Hall, Englewood Cliffs, NJ, 1956).
- ⁷⁸M. C. Beard, G. M. Turner, and C. A. Schmuttenmaer, *Phys. Rev. B* **62**, 15764 (2000).
- ⁷⁹T.-I. Jeon and D. Grischkowsky, *Phys. Rev. Lett.* **78**, 1106 (1997).
- ⁸⁰D. Shahar, D. C. Tsui, M. Shayegan, E. Shimshoni, and S. L. Sondhi, *Phys. Rev. Lett.* **79**, 479 (1997).
- ⁸¹D. Shahar, M. Hilke, C. C. Li, D. C. Tsui, S. L. Sondhi, J. E. Cunningham, and M. Razeghi, *Solid State Commun.* **107**, 19 (1998).
- ⁸²P. Phillips and C. Chamon, *Phys. Rev. Lett.* **95**, 107002 (2005).
- ⁸³M. R. Norman and A. V. Chubukov, *Phys. Rev. B* **73**, 140501(R) (2006).